Available online at www.sciencedirect.com

jmr&t Journal of Materials Research and Technology

journal homepage: www.elsevier.com/locate/jmrt

Hot deformation behavior of $0.5Y_2O_3/Al_2O_3$-Cu/30Mo3SiC composites doped with reduced graphene oxide

Hanjing Zhu [a,1], *Meng Zhou* [a,b,***,1], *Ke Jing* [a,b], *Baohong Tian* [a,b,**], *Yi Zhang* [a,b,*], *Xu Li* [c], *Yunzhang Li* [a], *Xianhua Zheng* [a], *Heng Li* [a], *Zipeng Ma* [a], *Yong Liu* [a,b], *Alex A. Volinsky* [d], *Jin Zou* [e]

[a] *Provincial and Ministerial Co-Construction of Collaborative Innovation Center for Non-Ferrous Metal New Materials and Advanced Processing Technology, School of Materials Science and Engineering, Henan University of Science and Technology, Luoyang 471023, China*

[b] *Henan Key Laboratory of Nonferrous Materials Science and Processing Technology, Luoyang 471023, PR China*

[c] *Center for Advanced Measurement Science, National Institute of Metrology, Beijing 100029, China*

[d] *Department of Mechanical Engineering, University of South Florida, 4202 E. Fowler Ave. ENG030, Tampa 33620, USA*

[e] *Jiangxi Key Laboratory for Advanced Copper and Tungsten Materials, Jiangxi Academy of Sciences, Nanchang 330096, China*

ARTICLE INFO

Article history:
Received 5 August 2023
Accepted 4 September 2023
Available online 9 September 2023

Keywords:
Copper matrix composites
Reduced graphene oxide
Hot deformation behavior
Al_2O_3
SiC

ABSTRACT

The $0.5Y_2O_3/Al_2O_3$-Cu/30Mo3SiC and 0.3GO-$0.5Y_2O_3/Al_2O_3$-Cu/30Mo3SiC composites were fabricated by fast hot press sintering. Hot compression tests of the composites were carried out using the Gleeble-1500 simulator at 0.001–10 s^{-1} strain rates and 650–950 °C deformation temperatures. The effects of doped reduced graphene oxide (rGO) on the hot deformation behavior and microstructure of $0.5Y_2O_3/Al_2O_3$-Cu/30Mo3SiC composites were investigated. Trace of molybdenum carbide (MoC) layers/nanoparticles formed in-situ at the rGO-Cu/Mo interface, which is beneficial to the interfacial bonding of the composite. The enhanced flow stress and activation energy of hot deformation is attributed to the addition of the rGO. The activation energy of the composites was improved by 11% with the addition of rGO. The dislocation density and texture orientation ratio decrease at higher deformation temperatures.

© 2023 The Authors. Published by Elsevier B.V. This is an open access article under the CC BY-NC-ND license (http://creativecommons.org/licenses/by-nc-nd/4.0/).

* Corresponding author. Provincial and Ministerial Co-Construction of Collaborative Innovation Center for Non-Ferrous Metal New Materials and Advanced Processing Technology, School of Materials Science and Engineering, Henan University of Science and Technology, Luoyang 471023, China

** Corresponding author. Provincial and Ministerial Co-Construction of Collaborative Innovation Center for Non-Ferrous Metal New Materials and Advanced Processing Technology, School of Materials Science and Engineering, Henan University of Science and Technology, Luoyang 471023, China

*** Corresponding author. Provincial and Ministerial Co-Construction of Collaborative Innovation Center for Non-Ferrous Metal New Materials and Advanced Processing Technology, School of Materials Science and Engineering, Henan University of Science and Technology, Luoyang 471023, China.

E-mail addresses: zhoumeng0902@126.com (M. Zhou), bhtian007@163.com (B. Tian), yizhang@haust.edu.cn (Y. Zhang).

[1] These authors contributed equally to this work.

https://doi.org/10.1016/j.jmrt.2023.09.031

2238-7854/© 2023 The Authors. Published by Elsevier B.V. This is an open access article under the CC BY-NC-ND license (http://creativecommons.org/licenses/by-nc-nd/4.0/).

1. Introduction

It is well known that composites prepared by adding a second phase to the matrix have good overall properties [1,2]. Copper has good electrical, thermal and corrosion resistance and is easy to process and mold [3,4]. Copper matrix composites (CMCs) can be obtained by adding different second phase elements to the Cu matrix. CMCs are commonly used in vacuum high-voltage switches and transformers with their excellent electrical and thermal conductivity [5–7]. However, the mechanical properties exhibited by copper matrix composites still have some room for improvement.

Carbon nanofillers such as graphene (Gr) [8–10], carbon nanotubes (GNTs) [11–13], carbon fibers (CFs) [14,15], and reduced graphene oxide (rGO) [16–18] can effectively enhance the comprehensive performance of the composites through the addition of carbon nanofillers to CMCs. Gr has a larger specific surface area and is more easily dispersed into the matrix compared to CNT, which allows for better transfer of its properties into the composite. However, it is an obvious problem is that the poor interfacial wettability and poor interfacial bonding between Gr and CMCs. It is difficult to obtain high-performance Gr-reinforced CMCs by simple preparation means, which always restricts their development [19]. The hydroxyl and carboxyl functional groups in graphene oxide (GO) can effectively improve the interfacial bonding with copper substrates. However, it has more internal oxygen-containing functional groups, which seriously affects the electrical conductivity of the composites [20]. The reduction of GO can effectively remove its internal functional groups and obtain rGO with better comprehensive performance. Combining rGO with copper matrix can enhance the mechanical properties of copper matrix composites. Dong et al. [21] improved the yield strength and tensile strength of W-Cu composites by 32.6% and 18.2%, respectively, by introducing rGO into W-Cu composites. Chu et al. [22] introduced rGO into CuCr composites and found that Cr_7C_3 layers/nanoparticles were generated in situ at the interface between rGO and Cr under high temperature environment, which improved the interfacial bonding of the composites. Yang et al. [23] investigated the effect of Ag and Ce modified rGO on the mechanical and electrical properties of CMCs and found that the hardness and electrical conductivity of the modified composites were significantly improved. Meanwhile, related studies have shown that the introduction of rGO into copper matrix electrical contact composites can effectively improve the arc erosion resistance of the composites. Dong et al. [24] reinforced CuW composites with Cu-modified rGO nano powders (i.e., Cu@rGO), and found that the fusion welding resistance of the composites was significantly improved, and the composites' resistance to arc erosion was improved. Copper matrix electrical contact composites are widely used in practice in a variety of electrical applications [25–27]. It is necessary to control the cost of their preparation. Powder metallurgy is an ideal preparation method, but it is still required to obtain the desired shape after hot processing. Inadequate exploration of the range of heat distortion processes will lead to significant energy consumption. Therefore, it is necessary to study the hot deformation behavior of composites.

The study of the hot deformation behavior of metals is an ongoing task for researchers [28,29]. Guan et al. [30] analyzed the deformation strengthening mechanism of graphene nanoplates and in-situ ZrB_2 nanoparticles reinforced AA6111 composites and found that GNPs and particle clusters promoted and hindered dynamic recrystallization (DRX). Wang et al. [31] investigated the hot deformation behavior of AA6061/B_4C composites and found that the main softening mechanism during hot deformation of this composite is dynamic recrystallization, and the lower the Z-value, the more likely DRX occurs. Deng et al. [32] investigated the hot deformation behavior of fine-grained SiC_p/AZ91 composites and found that the deformation mechanisms of SiC_p/AZ91 composites were different at different deformation rates. Ban et al. [33] investigated the effect of Cr addition on the hot deformation process of Cu alloys and found that Cr addition refines the grains and improves the activation energy of the alloy. Zhang et al. [34] prepared Al_2O_3-Cu/(W, Cr) composites by vacuum hot press sintering and internal oxidation. The effect of nanoparticles of Al_2O_3 and W on the hot deformation of Al_2O_3-Cu/(W, Cr) composites at different temperatures and strain rates was investigated. It was found that the flow stress increased with increasing strain rate and decreased with increasing deformation temperature. However, the role played by rGO in the hot deformation process of CMCs and the mechanism of its action have been rarely studied.

Previous work indicated that 0.5Y_2O_3/Al_2O_3-Cu/30Mo3SiC composites have excellent electrical contact properties [35]. On this basis, GO-reinforced 0.5Y_2O_3/Al_2O_3-Cu/30Mo3SiC composites were prepared in this study using powder metallurgical. However, composites are complicated and costly to prepare during practical application, and usually require secondary processing. The optimal hot processing range can be determined by studying the hot deformation behavior of composites. It is conducive to saving raw materials in actual production and promoting the optimal design of precision forming processes. Meanwhile, this work analyzes the hot deformation process of composites in depth using hyperbolic sine model, dynamic material model and electron backscatter diffraction (EBSD) to analyze the hot deformation mechanism of composites. This study provides reference for the practical production application of copper matrix electrical contact composites.

2. Experimental materials and procedures

2.1. Materials

The Cu-0.2 wt%Al alloy powder, Mo, Cu_2O, and SiC powder (Shanghai Bowei Applied Material Technology Co., Ltd., Shanghai, China) were used for the preparation of composites. Cu-0.2 wt%Al alloy powder was spherical and had 35–37 μm particle size with ≥99.9% purity. Mo powder was also spherical with 5–8 μm particle size and ≥99.95% purity. Cu_2O powder was spherical with 2–5 μm particle size and ≥99.95% purity. SiC powder had an irregular shape with 3–5 μm particle size and ≥99.95% purity. Spherical Y_2O_3 nano-powder (Jiangsu XFNANO Materials Tech Co., Ltd., Nanjing, China) had a 50 nm particle size with ≥99.99% purity. Single-layer GO

(Aladdin Reagent Co., Ltd., Shanghai, China) had 0.5–5 μm diameter, 0.8–1.2 nm thickness, and ≥99.9% purity.

2.2. Fabrication

The preparation of $0.5Y_2O_3/Al_2O_3$-Cu/30Mo3SiC and 0.3GO-$0.5Y_2O_3/Al_2O_3$-Cu/30Mo3SiC composites included ball milling, and sintering. Cu-0.2 wt%Al alloy, Cu_2O, Mo, SiC, and Y_2O_3 powder, and single-layer GO powder were weighed according to Table 1. The powder for the two composites were processed in the ball milling. In the ball milling process, to minimize the contamination of the composite powder, red copper balls were used as the medium. The tank was made of polymer material. No process control agent (PCA) was used [36,37]. The composite powder was obtained by ball milling using the QQM/B lightweight ball mill for 4 h. The ball-to-powder weight ratio was 3:1 [38,39]. The powder of two composites were sintered in a fast hot pressing sintering furnace (FHP-828). The vacuum in the furnace was kept below 10 Pa. The sintering pressure was 45 MPa. The heating rate was 100 °C/min. The samples were first heated to 700 °C for 10 min and then to 950 °C for 10 min, and the composite billet was taken out when the furnace cooled to about 100 °C. The structure of GO and composites was characterized by the NIM-ZY-NM-CL-022 laser confocal Raman spectrometer.

2.3. Physical and mechanical properties

Before conducting the hot deformation experiments, the comprehensive properties of the composites were tested as follows: the dry and wet weights of the sintered state styles were tested using a hydrostatic balance (MS105). The actual densities were determined by Archimedes' drainage method.

Table 1 – The nominal composition of the composites wt.%.

Composites	Composition					
	Cu-0.2%Al alloy powder	Mo	SiC	Cu_2O	Y_2O_3	GO
$0.5Y_2O_3/Al_2O_3$-Cu/30Mo3SiC	64.7	30	3	1.8	0.5	–
0.3GO-$0.5Y_2O_3/Al_2O_3$-Cu/30Mo3SiC	64.4	30	3	1.8	0.5	0.3

The density was calculated by combining the theoretical density of the composites. The sintered composites were tested for electrical conductivity using a conductivity tester (Sigma 2008 B1). The sintered composites were hardness-tested using a Vickers' hardness tester (HV-100) with a load of 50 gf and a holding time of 10 s.

2.4. Characterization

The sintered specimens were cut into cylindrical samples with Φ8 mm × 10 mm dimensions. The isothermal compression tests of the 0.3GO-$0.5Y_2O_3/Al_2O_3$-Cu/30Mo3SiC composite was performed using the Gleeble-1500 deformation simulator, as shown schematically in Fig. 1(a). The test temperature range was 650–950 °C, and the strain rate was 0.001–10 s^{-1}. Simultaneously, the action mechanism of rGO in the hot deformation process of CMCs was studied at the experimental conditions. To ensure uniform heating of the composites during hot compression, it was necessary to hold the composites for 3–5 min at high temperatures in the early stage of deformation. To preserve the high-temperature structure, water quenching was required quickly after compression was completed. To analyze the microstructure after hot deformation, transmission electron microscopy (TEM) and electron backscatter diffraction (EBSD) samples were cut by electrical discharge machining (EDM) along the direction perpendicular to the hot compression in Fig. 1(b–d) for subsequent characterization. After the samples were hand-polished to about 80 nm, Gatan 695 ion miller was used for TEM sample preparation. TEM, high-resolution transmission electron microscopy (HRTEM), and energy dispersive spectroscopy (EDS) images were obtained by FEI Tecani F30 transmission electron microscope. The EDS used was Oxford Xplore 80 mm^2. A JMS-7800F field emission scanning electron microscope (FESEM) with a step size of 0.5 μm and 20 kV voltage was used to obtain EBSD images. Channel 5 software was used to analyze the EBSD data.

3. Results and discussion

3.1. Physical and mechanical properties

The comprehensive properties of the two composites were tested before conducting the hot deformation experiments,

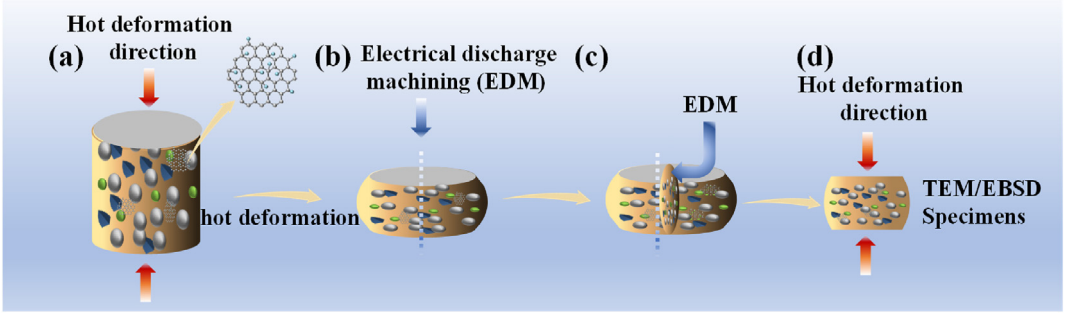

Fig. 1 – Schematic illustration of the hot deformation tests and the microstructure characterization. (a) Direction of hot compression test, (b) direction of electrical discharge machining, (c) TEM/EBSD specimens were taken at the cutting section, (d) TEM/EBSD specimens.

Table 2 – Mechanical and physical properties of copper matrix composites.

Composites	Relative density/ %	Electrical conductivity/% IACS	Vickers hardness/ HV	Compressive strength/ MPa
$0.5Y_2O_3$/Cu-Al_2O_3/30Mo/3SiC	98.46	51.59	206	471
0.3GO-$0.5Y_2O_3$/Cu-Al_2O_3/30Mo/3SiC	99.82	55.34	217	474

and the test results are shown in Table 2. The densities of both composites reached more than 98.4%. The electrical conductivity of the composites increased from 51.59 %IACS to 55.34 % IACS after the addition of GO. The microhardness of the composites increased from HV 206 to HV 217 with an increase of 5.34% after the addition of GO. The hardness of the composites was significantly enhanced by compositional design as compared to the work by Zhang et al. [34]. The increase in composite properties is favorable to improve the electrical contact properties of the composites.

3.2. *Microstructure*

The microstructure of the composites after hot deformation was characterized to analyze their thermodynamic properties after adding GO. Fig. 2 shows the interface structure of the 0.3GO-$0.5Y_2O_3$/Al_2O_3-Cu/30Mo3SiC composite deformed at 850 °C and 0.01 s^{-1} strain rate. For the Cu and Mo crystalline grain, the fast Fourier transform (FFT) image shows the (002), $(0\bar{1}1)$ and $(1\bar{1}\,\bar{1})$ diffraction patterns of Cu, and the $(01\bar{1})$, (020), and (011) diffraction pattern of Mo in Fig. 2(a), which also presents selected area electron diffraction (SAED). According to the noise-filtered inverse fast Fourier transform (IFFT) image, the lattice inter-planar spacing was 0.221 nm, best matching with the interplanar spacing of $(110)_{Mo}$. The spacing between $(1\bar{1}1)_{Cu}$ crystal planes of copper are 0.183 nm in Fig. 2(b and c). At the same time, the IFFT spots in Fig. 2(c) of the matrix and the secondary phase reveal many edge dislocations in the interior of the grains, which may be due to the extrusion effect of hot deformation on the grains. Dislocation multiplication will increase the flow stress and activation energy of composites. Fig. 2(d) shows the scanning transmission electron microscopy (STEM) image of a part of the region and the corresponding energy dispersive spectra of different elements. Fig. 2(e) is the FFT image corresponding to the selected region in Fig. 2(d), showing the diffraction patterns of the $(12\bar{1})$, $(3\bar{1}0)$ and (211) Y_2O_3 planes. Y_2O_3 is found at the interface between Mo and SiC. The existence of Y_2O_3 hinders the free growth of grains to a certain extent and plays a role in grain refinement [40].

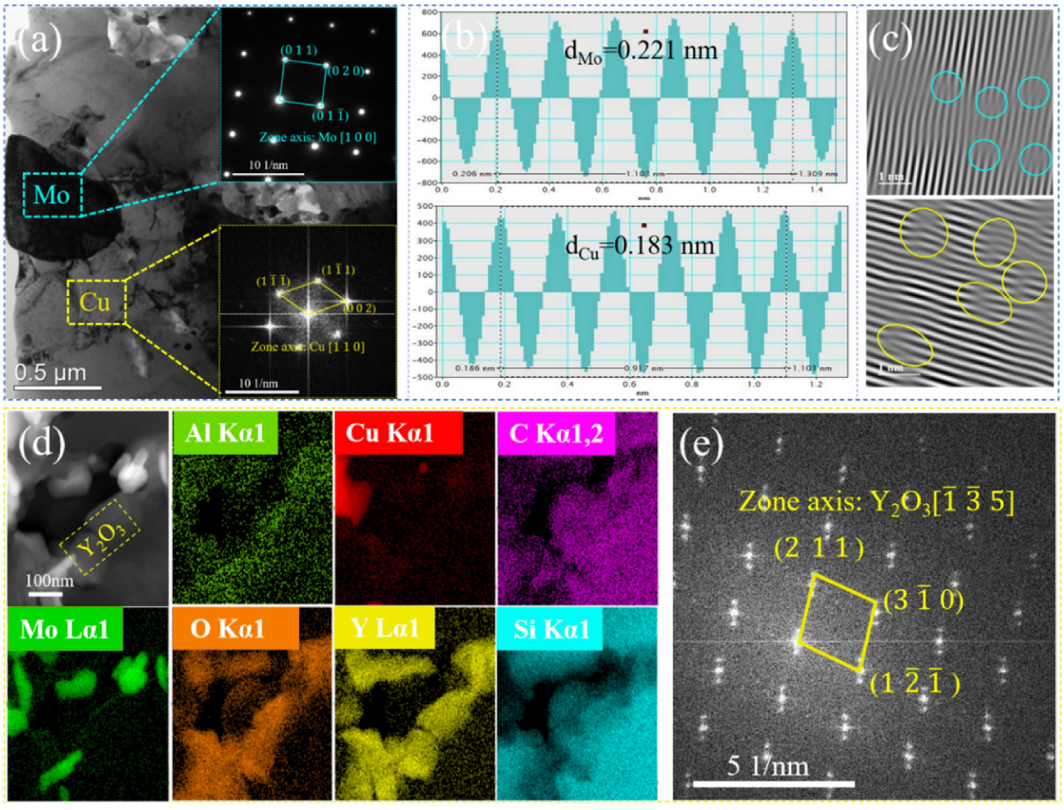

Fig. 2 – TEM images of the 0.3GO-$0.5Y_2O_3$/Al_2O_3-Cu/30Mo3SiC composite deformed at 850 °C and 0.01 s^{-1}. (a) HRTEM image and SAED of Mo and Cu, (b) corresponding lattice spacing measurements recorded at the marked regions in (a), (c) IFFT of the corresponding regions in (a), (d) HRTEM image of grains and EDS mapping of the different elements, (e) SAED of the corresponding regions in (d).

A twin boundary (TB) is a special low-energy interface, and its interfacial energy is about 10% of a normal large-angle grain boundary. Twin boundaries can be as effective as large-angle grain boundaries in blocking dislocation motion. Fig. 3 shows the microstructure of the 0.3GO-0.5Y_2O_3/Al_2O_3-Cu/30Mo3SiC composite deformed at 850 °C and 0.01 s^{-1} strain rate. Twin crystals were found in the 0.3GO-0.5Y_2O_3/Al_2O_3-Cu/30Mo3SiC composite after hot deformation. TB structure is further characterized by HRTEM and SAED. Some dislocation tangles and cells appear near the twin in Fig. 3(a). Since Cu has a face-centered cubic (fcc) structure, the twins in the Cu crystal are mainly caused by the stacking order change of the densely packed {111} planes. Both sides of the close-packed surface are symmetrically arranged in Fig. 3(b), showing a typical TB structure. The SAED pattern in Fig. 3(c) shows two sets of diffraction spots symmetrical about common {111} planes, further confirming a representative TB structure. Under the action of hot deformation, many dislocation tangles are formed in the matrix in Fig. 3(d). Dislocation accumulation will form a certain amount of energy at the defect, form dislocation walls through rearrangement, develop into small angle grain boundaries, and further develop into sub-grain in Fig. 3(e), thus greatly reducing dislocation density, which is typical recovery and recrystallization. At the same time, many nanoparticles were found to pin dislocations in the copper matrix, which hindered the dislocation movement. After FFT, diffraction patterns from the $(1\bar{1}\,\bar{1})$, (200), and (111) Cu planes and the $(31\bar{1})$, (222) and $(\bar{1}13)$ γ-Al_2O_3 planes were obtained in Fig. 3(f).

The structure of GO in 0.3GO-0.5Y_2O_3/Al_2O_3-Cu/30Mo3SiC composite was analyzed by Raman spectroscopy. Fig. 4 shows the Raman spectra of GO and 0.3GO-0.5Y_2O_3/Al_2O_3-Cu/30Mo3SiC composite, where the disorder peaks are represented by the D peak, and the G peak refers to tangential peaks [41]. The high-intensity ratio of D to G peaks and the high intensity of the D peak indicate the removal of some oxygen functional groups and the recovery of sp^2 carbon [42]. The higher intensity ratio of the D to G peaks (0.99 < 1.62) demonstrates successful generation of rGO.

The strengthening mechanism of rGO in the 0.3GO-0.5Y_2O_3/Al_2O_3-Cu/30Mo3SiC composite was studied by HRTEM, FFT, and IFFT. Fig. 5 shows the microstructure around rGO of the 0.3GO-0.5Y_2O_3/Al_2O_3-Cu/30Mo3SiC composite. Fig. 5(a) shows the TEM image of this area. Fig. 5(b) shows the HRTEM of the region corresponding to Fig. 5(a), showing a typical honeycomb structure of rGO. Fig. 5(b) was characterized by FFT, which further verified the existence of rGO in this region. Interestingly, some fine 100 nm particles were found around rGO by TEM. After indexing their diffraction spots, these particles are identified as MoO_3, and the size of Mo particles in the composite feedstock is 5–8 μm, indicating that there is a refinement of Mo particles in the process of composite preparation. The reasons for the refinement will be investigated in future work. After FFT, the $(13\bar{1})$, $(0\bar{5}\,\bar{1})$ and $(\bar{1}\,\bar{2}0)$ planes' diffraction patterns of MoO_3 were indexed. The rGO is also found in the gap between Mo and MoO_3 in Fig. 5(e). MoC is generated at the Mo/rGO and MoO_3/rGO interfaces, based on FFT and IFFT. Fig. 5(e_1) shows the (104) diffraction spots of MoC generated by Mo and rGO. The corresponding IFFT image in Fig. 5(e_2) depicts clear lattice fringes with a measured crystal plane spacing of 0.212 nm, corresponding to

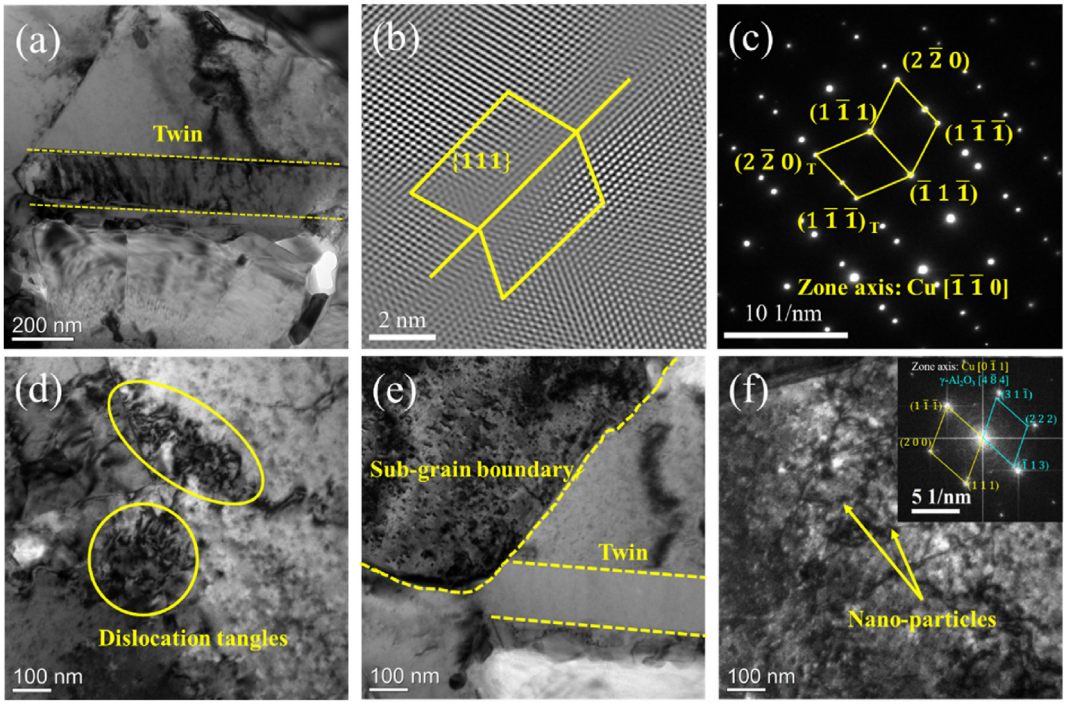

Fig. 3 – Microstructure of the 0.3GO-0.5Y_2O_3/Al_2O_3-Cu/30Mo3SiC composite deformed at 850 °C and 0.01 s^{-1}. (a) A twin, (b) the atomic arrangement of a representative twin boundary in FFT-treated HRTEM, (c) typical SAED pattern of Mo TBs, (d) dislocations tangles, (e) sub-grain boundary and a twin, (f) nanoparticles pinned dislocations and the corresponding SAED pattern.

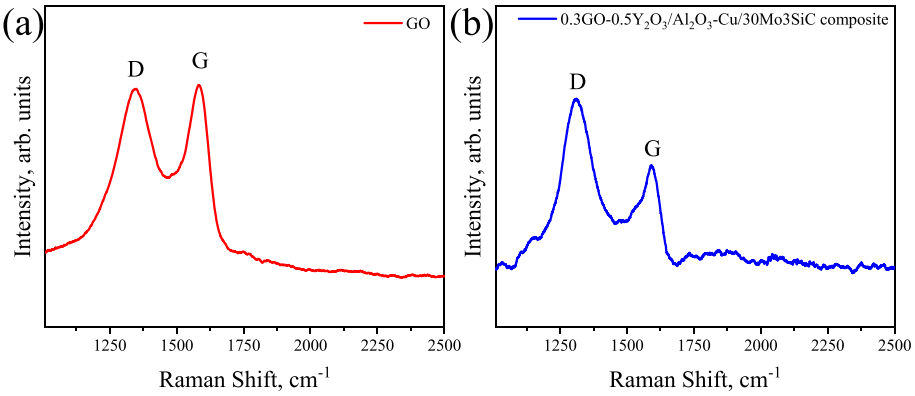

Fig. 4 – Raman spectra of the different materials. (a) GO and (b) $0.5Y_2O_3/Al_2O_3$-Cu/30Mo3SiC composite.

the MoC (104) plane. Fig. 5(e_3) shows the $(01\bar{5})$, (100), and $(1\bar{1}5)$ diffraction spots of MoC generated by MoO_3 and rGO along the $[0\bar{5}\bar{1}]$ band axis. The lattice arrangement directions of $(01\bar{5})_{MoC}$, $(100)_{MoC}$, and $(1\bar{1}5)_{MoC}$ are shown in Fig. 5(e_4). Interestingly, a honeycomb structure was found in the D region at the edge of rGO and MoO_3, which is a typical morphology of monolayer rGO. The reduced rGO in the composite loses the C atom to combine with Mo in MoO_3 to generate MoC layers/nanoparticles. The pinning effects of MoC layers/nanoparticles make Mo/MoO_3 bind more closely to rGO and the interfacial bonding between rGO and the metal matrix is further improved. Compared with the work of Manrique et al. [19], the generation of MoC allowed for a tighter bonding between rGO and the substrate. The poor wettability between graphene and metal substrate was improved and the interfacial relationship was optimized.

On the one hand, the existence of rGO acts as a bridge, connecting metal particles, making these hard phases harder to separate. On the other hand, rGO combines with metal particles to generate carbides and pins the interface to form a

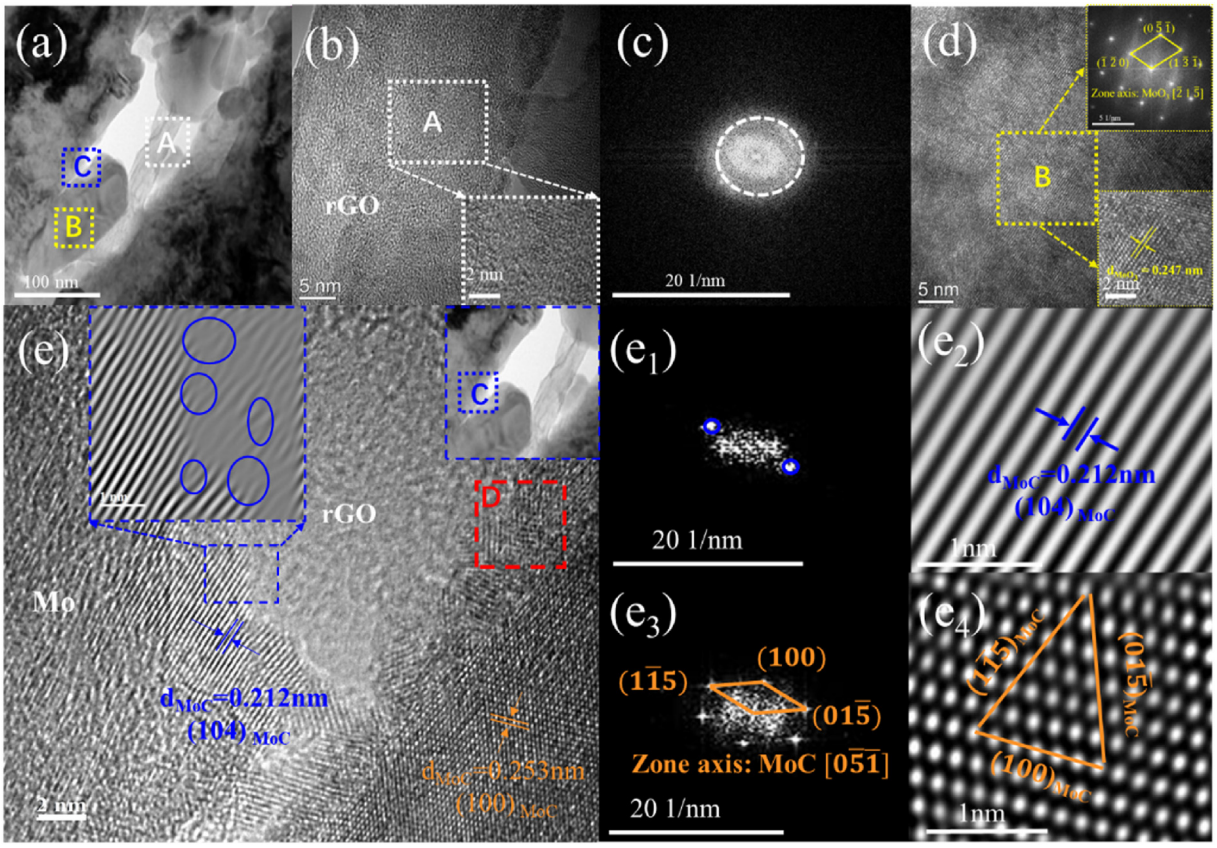

Fig. 5 – HRTEM images of the 0.3GO-$0.5Y_2O_3/Al_2O_3$-Cu/30Mo3SiC composite deformed at 850 °C and 0.01 s^{-1}. (a) HRTEM image, (b) HRTEM image corresponding to region A in (a), (c) FFT of (b), (d) HRTEM image and FFT corresponding to region B in (a), (e) HRTEM image corresponding to region C in (a), (e_1-e_4) are the detailed analysis of (e).

better bond between rGO and metal. It can be seen from Fig. 5(e) that the dislocation slip is blocked at the interface, which is the hindrance of the dislocation movement [43]. The hindering effect of rGO on dislocation is helpful to improve the flow stress of composites. The effects of rGO on the flow stress and activation energy during the hot deformation of composites are analyzed below.

3.3. *True stress-true strain curves*

Fig. 6 shows the true stress-true strain curves of $0.5Y_2O_3/Al_2O_3$-Cu/30Mo3SiC and 0.3GO-$0.5Y_2O_3/Al_2O_3$-Cu/30Mo3SiC composites deformed at different temperatures and strain rates. The hot deformation process of composites mainly includes work hardening, dynamic recovery, and DRX [44]. Fig. 6(a) and (b) show the true stress-true strain curves of the two composites deformed at 850 °C and 950 °C. When the deformation temperatures are the same, the flow stress increases with the strain rate, indicating that both composites are strain rate sensitive materials. With the increase of strain rate, the dislocation density increases significantly, forming high-density dislocation entanglements and improving the flow stress. At the same time, the higher the strain rate, the shorter the dynamic softening time, and insufficient softening will also increase the flow stress. Fig. 6(c) and (d) show the true stress-true strain curves of the two composites deformed at 0.01 s^{-1} and 1 s^{-1} strain rates. When the strain rates are the same, the flow stress of the two composites decreases with the deformation temperature. This is because higher temperature increases dislocation and vacancy activity, making grain boundary easier to migrate, which is conducive to dynamic recovery and DRX, reducing the flow stress [45].

Comparing the true stress-true strain curves of the two composites under the same hot deformation conditions, the maximum flow stress of the 0.3GO-$0.5Y_2O_3/Al_2O_3$-Cu/30Mo3SiC composite is always higher. The flow stress is the minimum stress required to allow dislocation movement through the crystal. The formation of rGO increases the maximum flow stress of the composites. According to the microstructure characterization results, the presence of rGO can effectively inhibit dislocation motion, and the generation of MoC layer/nanoparticles also plays a role in pinning dislocations to a certain extent. In addition, some existing studies have also proven that the presence of graphene can inhibit dislocation motion [46,47].

3.4. *Activation energy and constitutive equations*

It is well known that activation energy is an important parameter to characterize the hot deformation behavior of materials. It is an energy threshold value that metal atoms need to cross when the material is undergoing high-temperature plastic deformation. The activation energy of $0.5Y_2O_3/Al_2O_3$-Cu/30Mo3SiC and 0.3GO-$0.5Y_2O_3/Al_2O_3$-Cu/30Mo3SiC composites was calculated based on the flow stress curves, and constitutive equations were established.

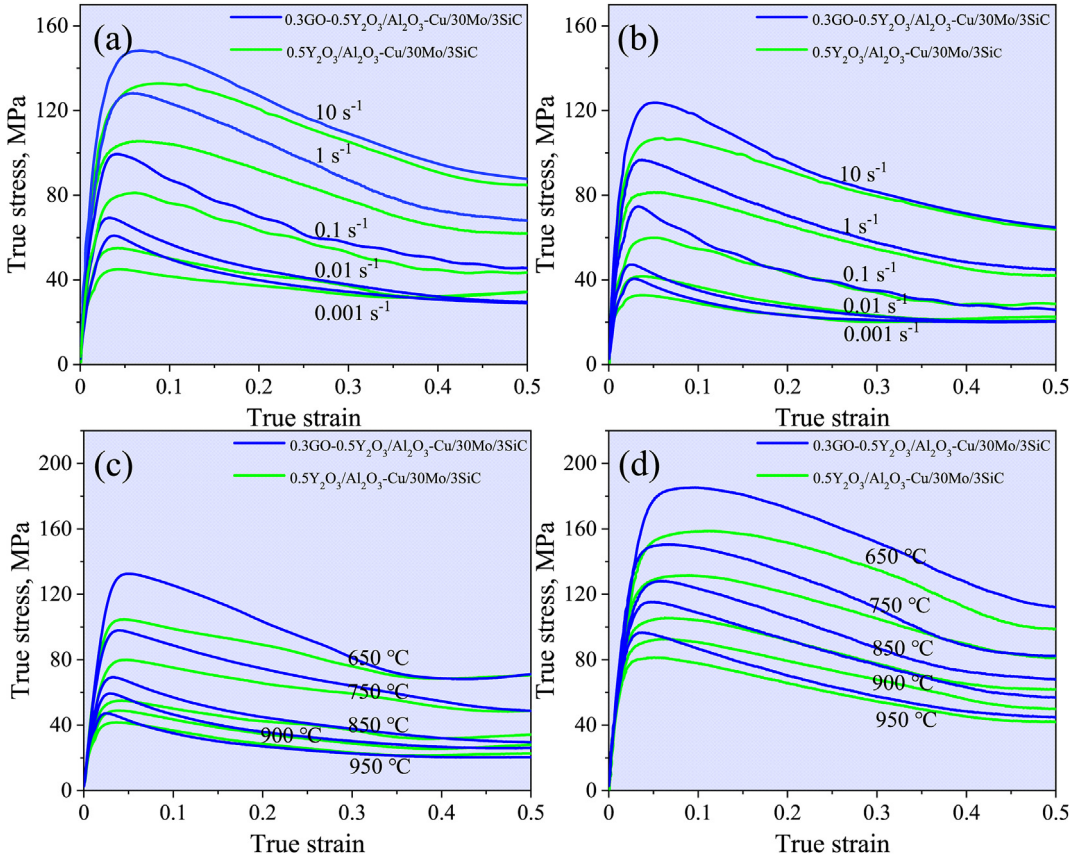

Fig. 6 – True stress-true strain curves of the $0.5Y_2O_3/Al_2O_3$-Cu/30Mo3SiC and 0.3GO-$0.5Y_2O_3/Al_2O_3$-Cu/30Mo3SiC composites deformed at different temperatures and strain rates: (a) 850 °C, (b) 950 °C, (c) 0.01 s^{-1}, (d) 1 s^{-1}.

The hyperbolic sine model proposed by Sellars and McTegart was adopted to link the flow stress, deformation temperature, and strain rate [48].

$$\dot{\varepsilon} = A_1 \sigma^{n_1} \exp\left(-\frac{Q}{RT}\right) \quad \alpha\sigma < 0.8 \tag{1}$$

$$\dot{\varepsilon} = A_1 \exp(\beta\sigma) \exp\left(-\frac{Q}{RT}\right) \quad \alpha\sigma > 1.2 \tag{2}$$

$$\dot{\varepsilon} = A[\sinh(\alpha\sigma)]^n \exp\left(-\frac{Q}{RT}\right) \text{(For all)} \tag{3}$$

Here, $\dot{\varepsilon}$ is the strain rate, σ is the peak stress in MPa, Q is the activation energy in J/mol, A, A_1, α, β, n_1, n, and R are constants, and T is the deformation temperature in K. Taking the natural logarithms of Eqs. (1)–(3):

$$\ln \dot{\varepsilon} = n_1 \ln \sigma + \ln A_1 - \frac{Q}{RT} \tag{4}$$

$$\ln \dot{\varepsilon} = \beta\sigma + \ln A_2 - \frac{Q}{RT} \tag{5}$$

$$\ln \dot{\varepsilon} = n \ln[\sinh(\alpha\sigma)] + \ln A - \frac{Q}{RT} \tag{6}$$

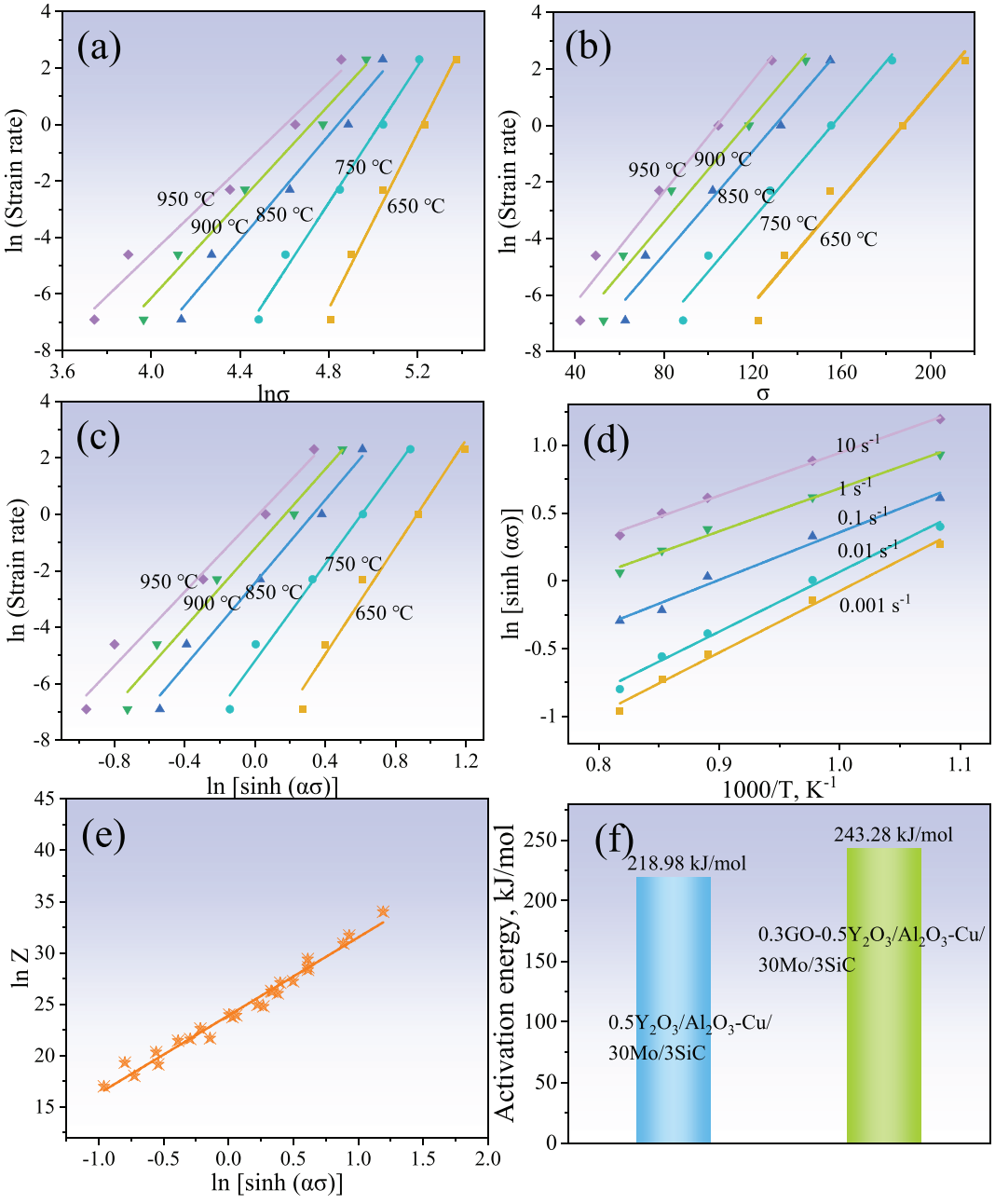

Fig. 7 – Relations between (a) ln(Strain rate) and lnσ, (b) ln(Strain rate) and lnσ, (c) ln(Strain rate) and ln[sinh($\alpha\sigma$)], (d) ln [sinh($\alpha\sigma$)] and 1000/T, (e) lnZ and ln[sinh($\alpha\sigma$)], (f) activation energy of the two composites.

To obtain the activation energy, we take partial derivatives of Eq. (3):

$$Q = R\left[\frac{\partial \ln \dot{\varepsilon}}{\partial \ln [\sinh(\alpha\sigma)]}\right]_T \left[\frac{\partial \ln[\sinh(\alpha\sigma)]}{\partial(1/T)}\right]_{\dot{\varepsilon}} = RnS \tag{7}$$

The Zenner-Hollomon parameter Z expresses the effects of deformation temperature and strain rate on the self-diffusion properties of the lattice during hot deformation:

$$Z = \dot{\varepsilon}\, exp\left[-\frac{Q}{RT}\right] \tag{8}$$

Substituting Eq. (8) into Eq. (3) and taking natural logarithms of both sides yields:

$$\ln Z = \ln A + n[\ln \sinh(\alpha\sigma)] \tag{9}$$

The peak stress obtained under different deformation conditions is used in Eq. (9), and the relationships between flow stress, strain rate, and deformation temperature are plotted in Fig. 7. Fig. 7(a–e) show the relationships between ln(Strain rate) and $\ln \sigma$, ln(Strain rate) and σ, ln(Strain rate) and ln[sinh(σ s)], ln [sinh(σ s)] and $T^{-1}/10^{-3}$ K^{-1} and lnZ and ln[sinh(σ s)] of the 0.3GO-0.5Y_2O_3/Al_2O_3-Cu/30Mo3SiC composite. In addition, n, n_1, β, and S are the average slopes in Fig. 7(a–d), which can be determined as $n = 7.80$, $n_1 = 10.60$, $\beta = 0.09$, and $S = 3.76$, respectively. According to Eq. (7), the intercept of the line lnZ-ln [sinh(σ s)] in Fig. 7(e) is lnA and the linear fitting results in $\ln A = 23.91$. Therefore, the activation energy of the 0.5Y_2O_3/Al_2O_3-Cu/30Mo3SiC composite is $Q = RnS = 218.98$ kJ/mol, and the activation energy of the 0.3GO-0.5Y_2O_3/Al_2O_3-Cu/30Mo3SiC composite is 243.28 kJ/mol. The activation energy of the composites was significantly improved comparison with the study of Li et al. [49]. Finally, the constitutive equations of the 0.5Y_2O_3/Al_2O_3-Cu/30Mo3SiC and 0.3GO-0.5Y_2O_3/Al_2O_3-Cu/30Mo3SiC composites can be given as follows.

For the 0.5Y_2O_3/Al_2O_3-Cu/30Mo3SiC composite:

$$\dot{\varepsilon} = e^{21.167}[\sinh(0.011\sigma)]^{6.84} \exp\left(-\frac{218980}{8.314T}\right) \tag{10}$$

For the 0.3GO-0.5Y_2O_3/Al_2O_3-Cu/30Mo3SiC composite:

$$\dot{\varepsilon} = e^{23.906}[\sinh(0.009\sigma)]^{7.8} \exp\left(-\frac{243275}{8.314T}\right) \tag{11}$$

Fig. 7(f) shows the activation energy of 0.5Y_2O_3/Al_2O_3-Cu/30Mo3SiC and 0.3GO-0.5Y_2O_3/Al_2O_3-Cu/30Mo3SiC composites.

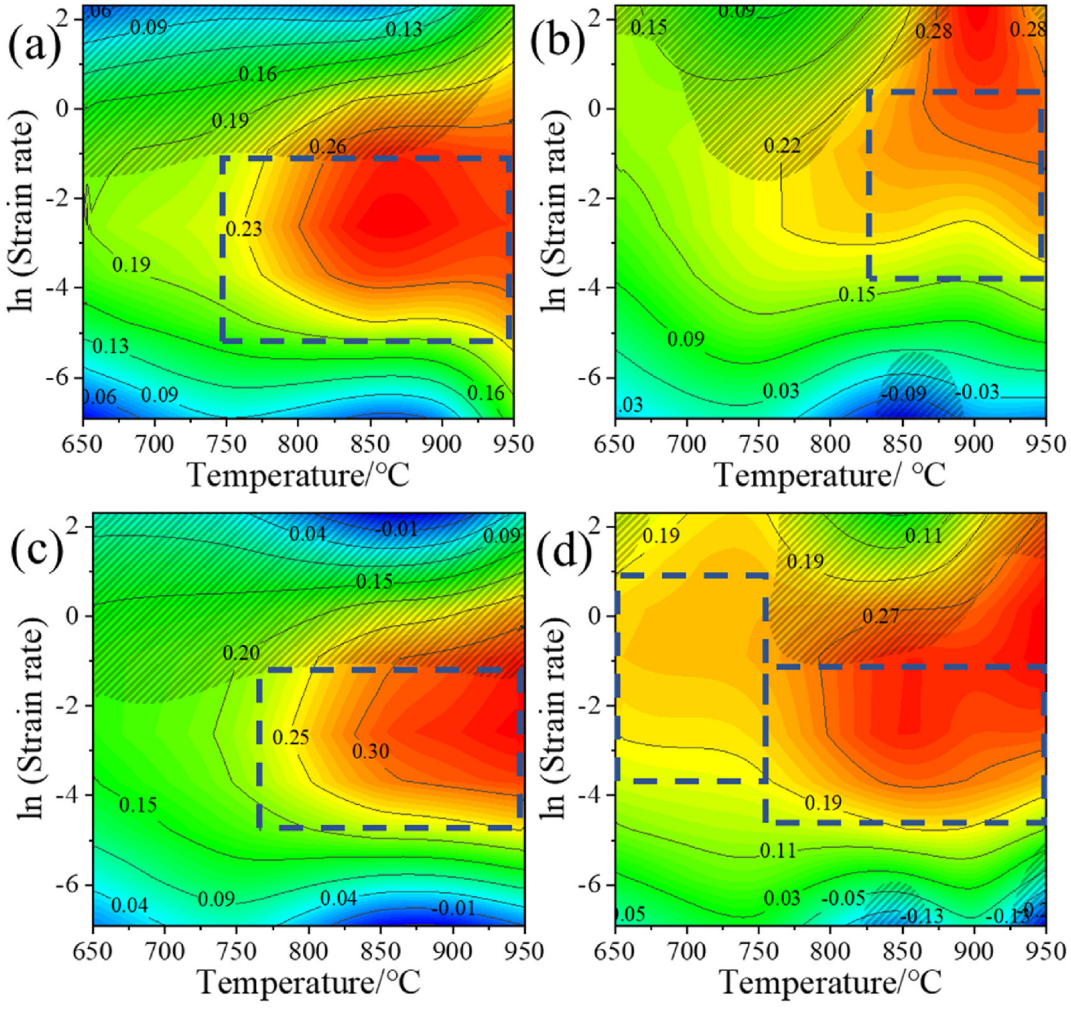

Fig. 8 – Hot processing maps. (a, b) 0.5Y_2O_3/Al_2O_3-Cu/30Mo/3SiC composites of 0.1 strain, (c, d) 0.3GO-0.5Y_2O_3/Al_2O_3-Cu/30Mo/3SiC composites of 0.5 strain.

The activation energy of the 0.3GO-0.5Y_2O_3/Al_2O_3-Cu/30Mo3SiC composite is 11% higher than the 0.5Y_2O_3/Al_2O_3-Cu/30Mo3SiC composite, which indicates that the addition of rGO improves the deformation resistance of the composite.

3.5. *Processing map analysis*

The hot processing map derived based on the dynamic material model (DMM), which is a superposition of the power dissipation efficiency map and the rheological instability map. It can well reflect the advantages and disadvantages of the hot processing performance of composites. The results of the hot processing map allow to obtain the most suitable processing areas in the composites, thus reducing the loss of raw materials in production applications. The number in the figure is the power dissipation coefficient 'η' of the composites at a certain temperature and deformation rate. The larger the value, the more stable the microstructure evolution of the material during the hot deformation process, and the better the hot processing performance of the material. The shadow area in the figure is the instability zone of the composites at a certain deformation temperature and deformation rate. The material in the instability zone is prone to holes and cracks, resulting in material failure. The best hot processing area of the material can be determined by the hot processing map, and the area represented by the blue box in the figure is the best processing range of the composites. Fig. 8(a and b) shows the hot processing diagrams of 0.5Y_2O_3/Al_2O_3-Cu/30Mo/3SiC composites at 0.1 and 0.5 strain with the corresponding hot compression parameters of strain rate 0.0053–0.2865 s^{-1} at

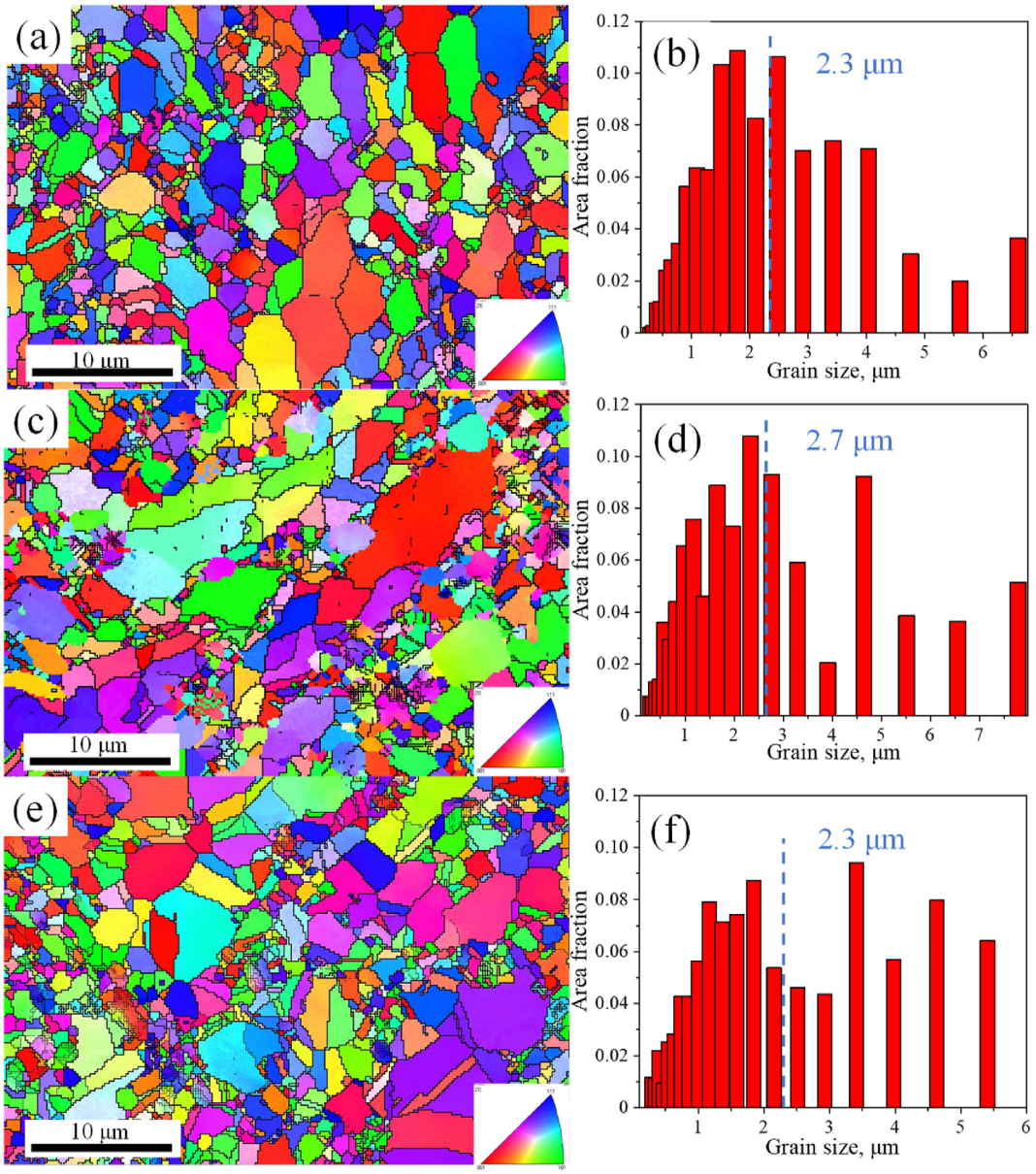

Fig. 9 – EBSD micrographs and grain size distribution of the composites under different deformation conditions. (a, b) 0.5Y_2O_3/Al_2O_3-Cu/30Mo3SiC deformed at 850 °C and 0.01 s^{-1} composite, (c, d) 0.3GO-0.5Y_2O_3/Al_2O_3-Cu/30Mo3SiC deformed at 850 °C and 0.01 s^{-1}, (e, f) 0.3GO-0.5Y_2O_3/Al_2O_3-Cu/30Mo3SiC deformed at 950 °C and 0.01 s^{-1}.

750–950 °C and strain rate 0.0202–1.4918 s^{-1} at 825–950 °C. Fig. 8(c and d) shows the hot processing of 0.3GO-0.5Y_2O_3/Al_2O_3-Cu/30Mo/3SiC composites at 0.1 and 0.5 strains with the corresponding hot compression parameters of strain rates 0.0067–0.2231 s^{-1} at 770–950 °C and 0.0821–2.2255 s^{-1} at 650–750 °C and strain rate 0.0183–0.3679 s^{-1} at 800–950 °C.

3.6. EBSD analysis

The grain size, shape, dislocation density, and texture evolution of composites under different deformation conditions were analyzed by the EBSD method. Fig. 9 shows the EBSD orientation and grain size distribution of the 0.3GO-0.5Y_2O_3/Al_2O_3-Cu/30Mo3SiC and 0.5Y_2O_3/Al_2O_3-Cu/30Mo3SiC composites deformed at different conditions. As seen in Fig. 9(a), (c), and (e), there are different amounts of recrystallized grains around the coarse deformed grains. The average grain size of the 0.5Y_2O_3/Al_2O_3-Cu/30Mo3SiC composite is smaller than the 0.3GO-0.5Y_2O_3/Al_2O_3-Cu/30Mo3SiC composite under the same deformation conditions in Fig. 9(b) and (d). This may be because the number of fines dynamically recrystallized grains in the 0.3GO-0.5Y_2O_3/Al_2O_3-Cu/30Mo3SiC composite is less than in the 0.5Y_2O_3/Al_2O_3-Cu/30Mo3SiC composite in Fig. 9(a) and (c). Meanwhile, the average grain size of the 0.3GO-0.5Y_2O_3/Al_2O_3-Cu/30Mo3SiC composite decreased from 2.7 μm to 2.3 μm at higher deformation temperature in Fig. 9(d) and (f). This is because the DRX of the composite is more complete at higher temperatures, as the coarse deformed grains were gradually replaced by recrystallized grains, and the average grain size decreased. Therefore, it can be concluded that the DRX of the 0.3GO-0.5Y_2O_3/Al_2O_3-Cu/30Mo3SiC composite is promoted by the increase in temperature.

The geometrically necessary dislocation (GND) can be quantitatively calculated from the kernel average misorientation (KAM) map. Higher values indicate higher dislocation density. The GND can be calculated as in [50]:

$$\rho^{GND} = \frac{2\theta}{\mu b} \tag{12}$$

Here, ρ^{GND} is the geometrically necessary dislocation in m^{-2}. θ is the mean orientation, μ is the scanning step size of 0.17 μm, and b is the Burgers vector of Cu (0.255 nm). ρ^{GND} can be obtained from the KAM map in Fig. 10. The GND of 0.5Y_2O_3/Al_2O_3-Cu/30Mo3SiC and 0.3GO-0.5Y_2O_3/Al_2O_3-Cu/30Mo3SiC composites deformed at 850 °C, 0.01 s^{-1} was calculated as 2.2×10^{15} m^{-2} and 2.8×10^{15} m^{-2}, respectively in Fig. 10(a) and (b). The GND of the composites is significantly improved compared to Liang et al. [34]. The GND of the composite was higher after the addition of GO at the same deformation temperature, indicating that the addition of GO could improve the dislocation density. However, the GND of the 0.3GO-0.5Y_2O_3/Al_2O_3-Cu/30Mo3SiC composite decreased to 1.8×10^{15} m^{-2} when the deformation temperature increased to 950 °C in Fig. 10(b) and (c). GND decreased with the deformation temperature, indicating that DRX will consume dislocations and reduce dislocation density. This is because DRX requires the consumption of energy stored by dislocations to provide the driving force for DRX nucleation.

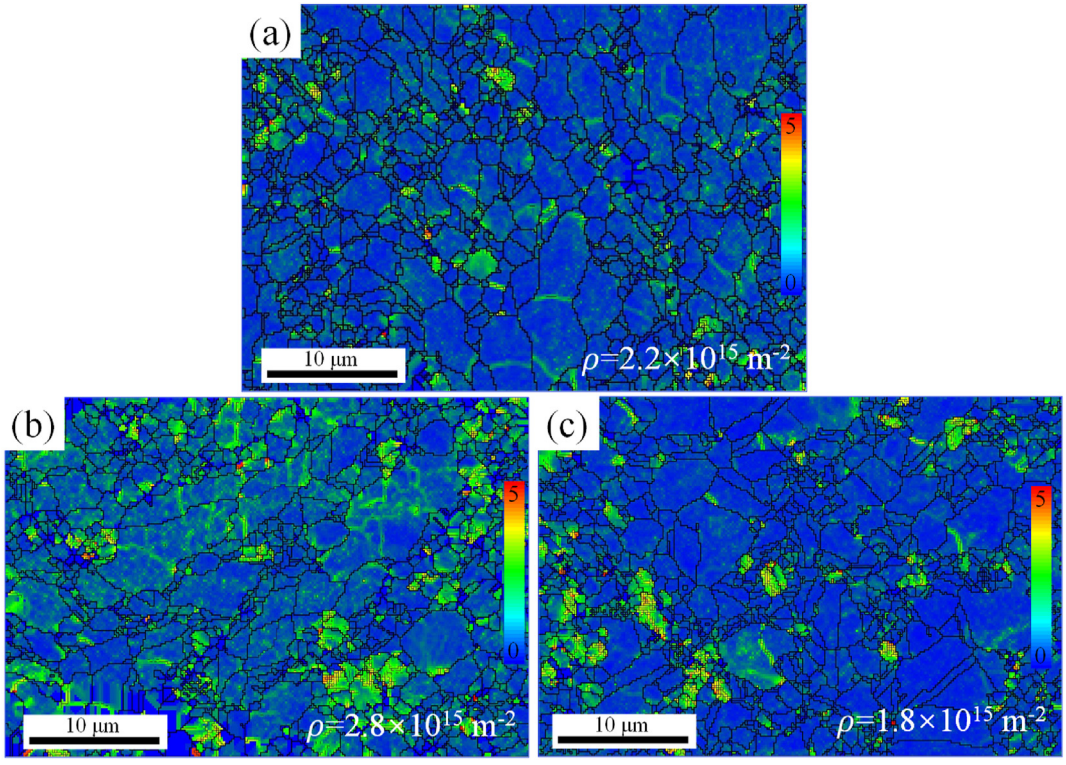

Fig. 10 – The KAM maps of the composites deformed at different conditions. (a) 0.5Y_2O_3/Al_2O_3-Cu/30Mo3SiC deformed at 850 °C and 0.01 s^{-1}, (b) 0.3GO-0.5Y_2O_3/Al_2O_3-Cu/30Mo3SiC deformed at 850 °C and 0.01 s^{-1}, (c) 0.3GO-0.5Y_2O_3/Al_2O_3-Cu/30Mo3SiC deformed at 950 °C and 0.01 s^{-1}.

Fig. 11 shows the EBSD grain boundary diagram and orientation angle distribution of the $0.5Y_2O_3/Al_2O_3$-Cu/30Mo3SiC and 0.3GO-$0.5Y_2O_3/Al_2O_3$-Cu/30Mo3SiC composites deformed at different conditions. The misorientation angle of high-angle grain boundaries (HAGBs) of the 0.3GO-$0.5Y_2O_3/Al_2O_3$-Cu/30Mo3SiC composite is lower than the $0.5Y_2O_3/Al_2O_3$-Cu/30Mo3SiC composite deformed under the same conditions in Fig. 11. This can be attributed to more deformed grains and higher dislocation density in the 0.3GO-$0.5Y_2O_3/Al_2O_3$-Cu/30Mo3SiC composite. This is because the addition of GO enhances the accumulation of dislocations and thus retards the onset of DRX. However, the percentage of 0.3GO-$0.5Y_2O_3/Al_2O_3$-Cu/30Mo3SiC composite HAGBs increased from 60% to 86% with temperature in Fig. 11(c–f). As can be seen from the KAM maps, dislocation consumption is required for DRX. Thus, it can be inferred that an increase in the misorientation angle of HAGBs means an increase in DRX and a decrease in the dislocation density. In composites, dynamic recovery, and DRX can be promoted by consuming low-angle grain boundaries (LAGBs) [51]. The dislocations caused by hot deformation gradually accumulate at LAGBs, leading to the increase of the misorientation angles and the formation of HAGBs. Thus, the grain boundaries of the recrystallized grains are HAGBs, and the sub-grains are surrounded by LAGBs.

Fig. 12 shows the recrystallized grains, sub-structured and deformed grains of the $0.5Y_2O_3/Al_2O_3$-Cu/30Mo3SiC and 0.3GO-$0.5Y_2O_3/Al_2O_3$-Cu/30Mo3SiC composites deformed at different conditions. Blue color represents recrystallized grains, yellow

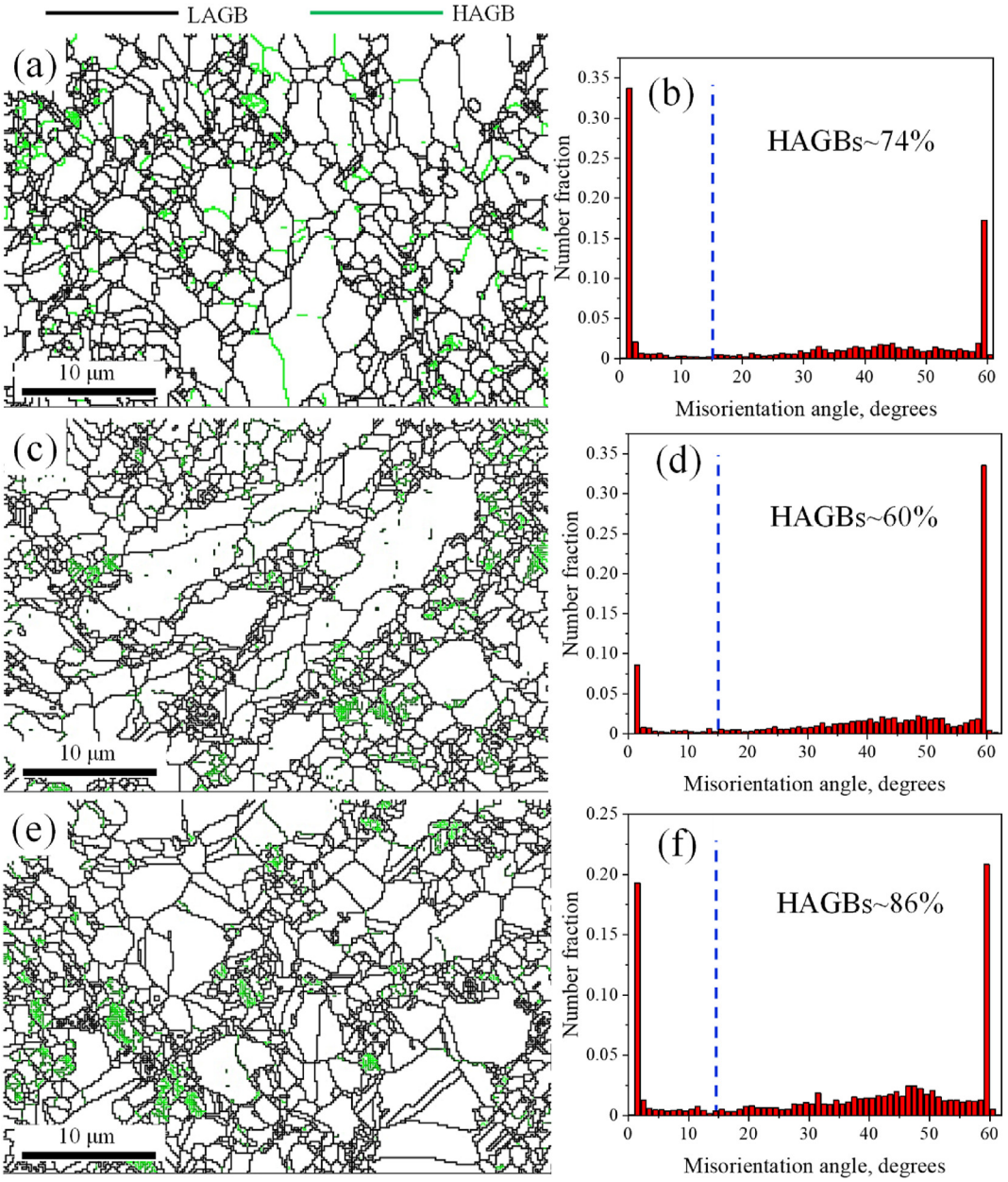

Fig. 11 – EBSD orientation maps and misorientation angle distribution of composites deformed under different conditions. (a, b) $0.5Y_2O_3/Al_2O_3$-Cu/30Mo3SiC deformed at 850 °C and 0.01 s^{-1}, (c, d) 0.3GO-$0.5Y_2O_3/Al_2O_3$-Cu/30Mo3SiC deformed at 850 °C and 0.01 s^{-1}, (e, f) 0.3GO-$0.5Y_2O_3/Al_2O_3$-Cu/30Mo3SiC deformed at 950 °C and 0.01 s^{-1}.

color represents sub-structured grains and red color represents deformed grains. It can be seen from Fig. 12(a–d) that the percentage of dynamically recrystallized grains decreased after the GO addition for the same deformation conditions. This indicates that the addition of GO retards the onset of DRX. The substructured grains dominate at 850 °C and the recrystallized grains dominate at 950 °C in Fig. 12(c–f). This shows that the increase in temperature promotes DRX and increases the number of recrystallized grains in the material, which is consistent with the results in Fig. 11.

At the same time, the texture evolution of the 0.3GO-0.5Y_2O_3/Al_2O_3-Cu/30Mo3SiC composite at different deformation temperatures was investigated by polar and inverse polar diagrams. In general, pole plots and antipole plots are usually represented by low crystal exponents, such as {111}, {110}, and {100}. In addition, the common recrystallization textures in fcc metals are the {011} <100> Goss texture, {112} <111> Copper texture, {111} <211> R texture, {001} <100> Cubic texture and {011} <211> Brass texture [52,53]. The texture strength of the composites decreases with the deformation temperature in Fig. 13. The maximum texture strength of the polar figure is reduced from 3.810 to 3.220, and the texture strength of the reverse polar figure is reduced from 2.127 to 1.545. This is because the increase in temperature promotes the DRX and makes the texture distribution more random. In general, with the increase of hot deformation temperature, the proportion of Cube, Goss, Brass, Copper, and S texture decreases, while <111>//X, <110>//X and <100>//X increased. According to the

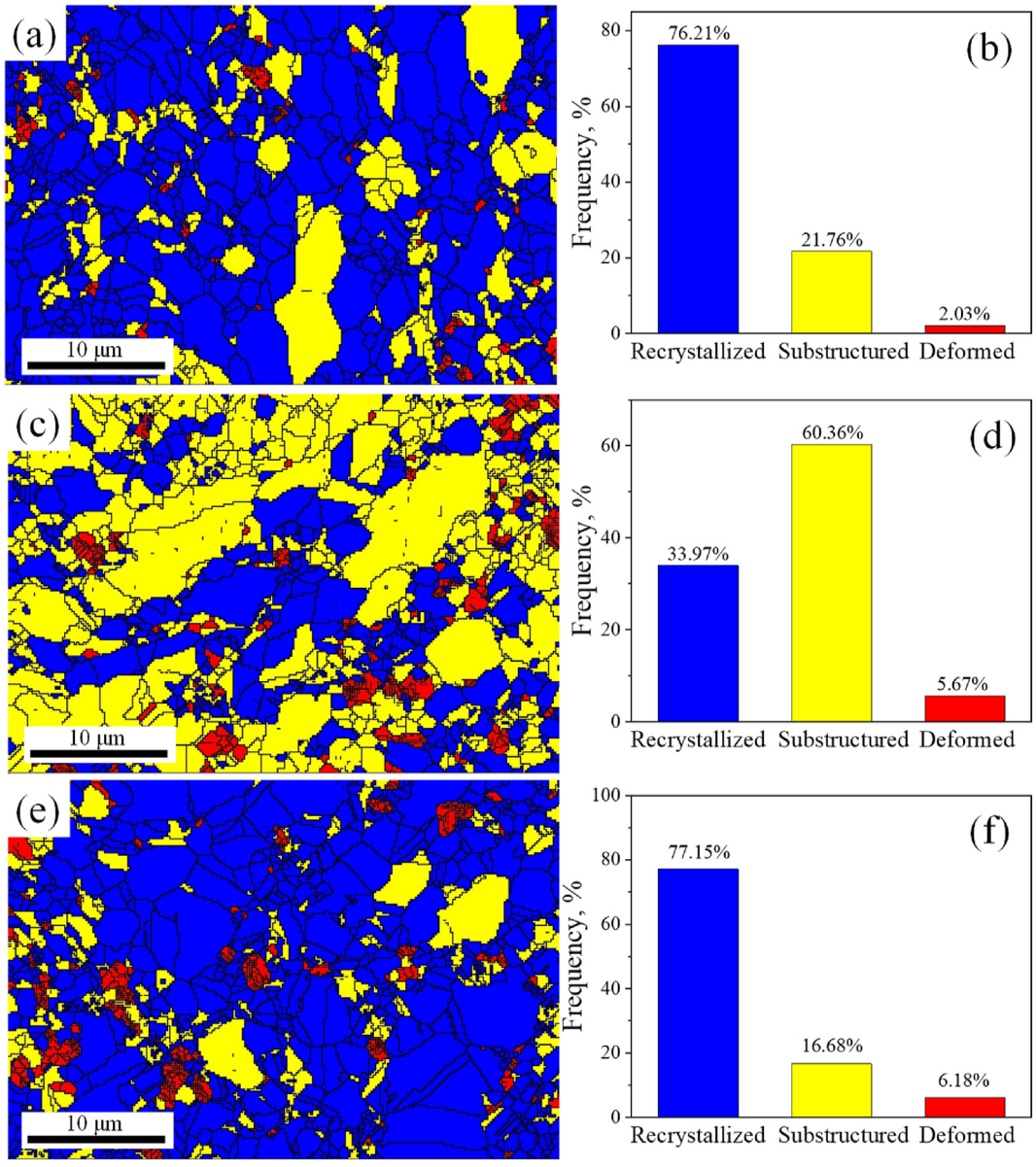

Fig. 12 – The recrystallized, substructured, deformed regions, and their frequency percentage in the composites under different deformation conditions. (a, b) 0.5Y_2O_3/Al_2O_3-Cu/30Mo3SiC deformed at 850 °C and 0.01 s^{-1}, (c, d) 0.3GO-0.5Y_2O_3/Al_2O_3-Cu/30Mo3SiC deformed at 850 °C and 0.01 s^{-1}, (e, f) 0.3GO-0.5Y_2O_3/Al_2O_3-Cu/30Mo3SiC deformed at 950 °C and 0.01 s^{-1}.

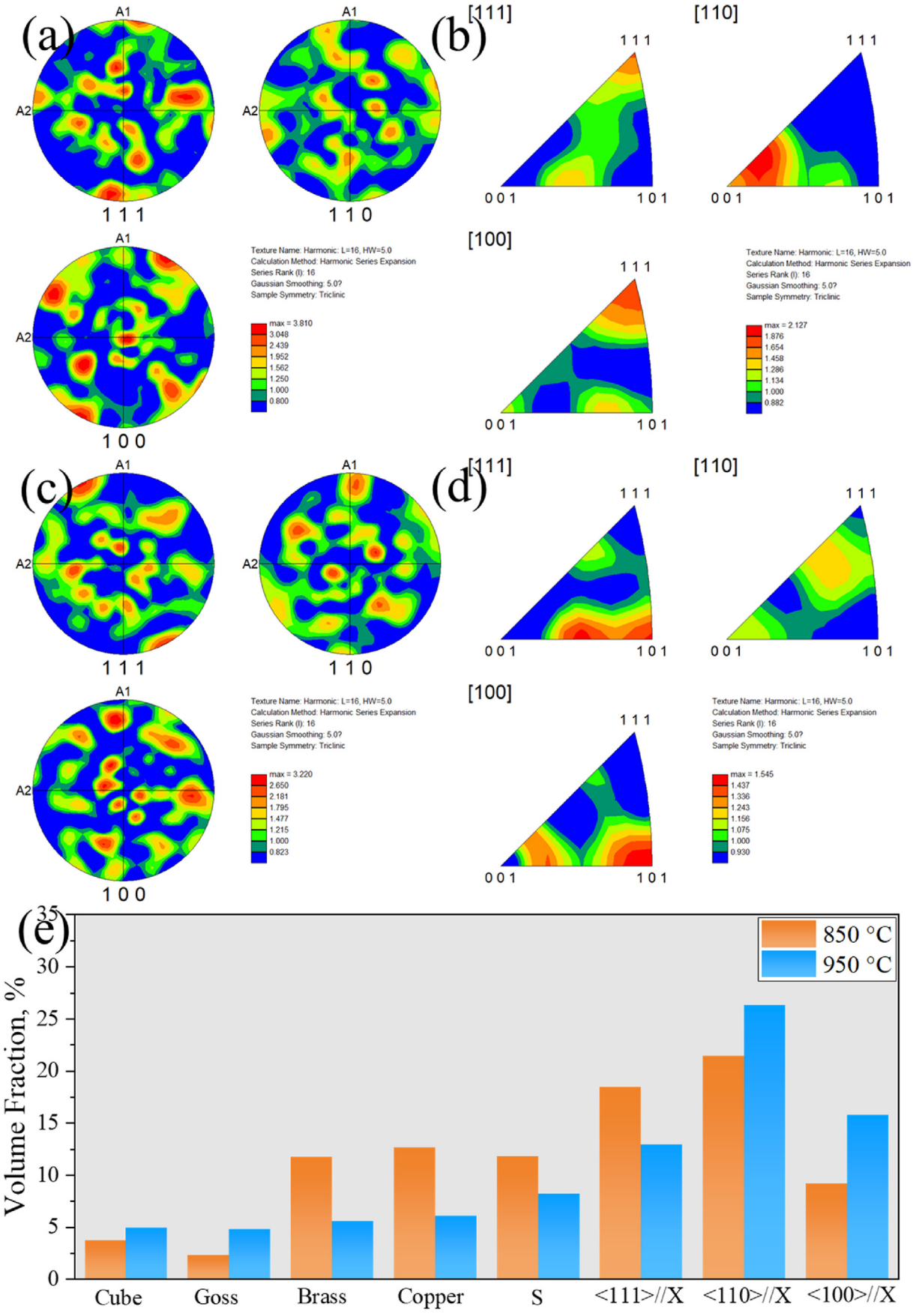

Fig. 13 – Pole figures, inverse pole figures, and texture volume fraction of the 0.3GO-0.5Y_2O_3/Al_2O_3-Cu/30Mo3SiC composite deformed at 0.01 s^{-1} strain rate and different temperatures. (a, b) 850 °C, (c, d) 950 °C, (e) the volume fraction of textures.

analysis of true stress-true strain curves and microstructure evolution, the change of texture orientation is due to DRX.

4. Conclusions

Hot compression of the $0.5Y_2O_3/Al_2O_3$-Cu/30Mo3SiC and $0.3GO\text{-}0.5Y_2O_3/Al_2O_3$-Cu/30Mo3SiC composites was conducted at the deformation temperature ranging from 650 °C to 950 °C and the strain rate ranging from 0.001 s^{-1} to 10 s^{-1}. The following conclusions can be drawn.

(1) The distribution of yttrium oxide in the grain boundary inhibits grain growth. The dispersion of γ-Al_2O_3 in the Cu matrix inhibits the dislocation movement, deformation twins conducive to the increase of the peak flow stress and activation energy of the composite.
(2) rGO was obtained by ball milling and FHP sintering. MoC layers/nanoparticles were formed in-situ at the rGO-Cu/Mo interface. MoC layers/nanoparticles and rGO inhibit dislocation motion during the hot deformation of the composite, which increases the activation energy by 11%.
(3) The optimal hot processing ranges for both composites at 0.1 and 0.5 strain were determined. Based on the hyperbolic sine model, the constitutive equations of the two composites were established.
(4) The addition of GO improves the GND of the composites. The DRX is promoted with the increase of temperature. The grain size, GND, HAGBs ratio, and texture strength decreased with the increase of hot deformation temperature.

Declaration of competing interest

The authors declare that they have no known competing financial interests or personal relationships that could have appeared to influence the work reported in this paper.

Acknowledgements

This work was supported by the National Natural Science Foundation of China (52071134, 52101083), the Program for Innovative Research Team at the University of the Henan Province (22IRTSTHN001), China Postdoctoral Science Foundation (2023TQ0107), Technology Innovation Center of Graphene Metrology and Standardization for State Market Regulation (No. AKYKF2309), Key Research and Development Program of Jiangxi Province, China (20224BBE52002).

REFERENCES

[1] Biyik S. Characterization of nanocrystalline Cu25Mo electrical contact material synthesized via ball milling. Acta Phys Pol, A 2017;132(3):886–8.
[2] Biyik S. Effect of cubic and hexagonal boron nitride additions on the synthesis of Ag-SnO2 electrical contact. Material. J Nanoelectron Optoe 2019;14(7):1010–5.
[3] Guler O, Varol T, Alver U, Biyik S. The wear and arc erosion behavior of novel copper based functionally graded electrical contact materials fabricated by hot pressing assisted electroless plating. Adv Powder Technol 2021;32(8):2873–90.
[4] Biyik S. Effect of reinforcement ratio on physical and mechanical properties of Cu-W composites synthesized by ball milling. Mater Focus 2018;7(4):535–41.
[5] Jamwal A, Mittal P, Agrawal R, Gupta S, Kumar D, Sadasivuni KK, et al. Towards sustainable copper matrix composites: manufacturing routes with structural, mechanical, electrical and corrosion behavior. J Compos Mater 2020;54(19):2635–49.
[6] Lech M, Wgierek P, Kozak C, Pastuszak J. Methodology for testing the electric strength of vacuum chambers designed for modern medium voltage switchgear. Metrol Meas Syst 2021;27(4):687–700.
[7] Nachiketa R, Bernd K, Mützel T, Froyen L, Vanmeensel K, Vleugels J. Effect of WC particle size and Ag volume fraction on electrical contact resistance and thermal conductivity of Ag-WC contact materials. Mater Des 2015;85:412–22.
[8] Wang M, Sheng J, Wang LD, Wang G, Fei W. Achieving high strength and electrical properties in drawn fine Cu matrix composite wire reinforced by in-situ grown graphene. J Mater Res Technol 2022;17:3205–10.
[9] Guo SY, Zhang X, Shi CS, Zhao DD, He CN, Zhao NQ. Fully exploiting the role of heterogeneous grain structure in graphene nanoplatelets reinforced Cu matrix composites through interfacial structure design. Compos Commun 2022;35:101287.
[10] Ali S, Ahmad F, Yusoff PSMM, Muhamad N, Oñate E, Raza RM, et al. A review of graphene reinforced Cu matrix composites for thermal management of smart electronics. Composer Part A-Appl S 2021;144:106357.
[11] Wei X, Tao JM, Hu Y, Liu YC, Bao R, Li FX, et al. Enhancement of mechanical properties and conductivity in carbon nanotubes (CNTs)/Cu matrix composite by surface and intratube decoration of CNTs. Mater Sci Eng, A 2021;816:141248.
[12] Zhao Q, Gan XP, Zhou KC. Enhanced properties of carbon nanotube-graphite hybrid-reinforced Cu matrix composites via optimization of the preparation technology and interface structure. Powder Technol 2019;355:408–16.
[13] Long F, Guo XH, Song KX, Jia SG, Yakubov V, Li SL, et al. Enhanced arc erosion resistance of TiB_2/Cu composites reinforced with the carbon nanotube network structure. Mater Des 2019;183:108136.
[14] Jia CF, Li SL, Guo XH, Wang X, Su JH, Song KX. Arc erosion resistance mechanism of C_f-Al_2O_3/Cu composites modified by carbon fibers. J Mater Res Technol 2022;19:4957–68.
[15] Ali S, Ahmad F, Shirazi MI, Malik K, Raza MR, Memon IR. Flow induced fiber orientation in short carbon fiber reinforced copper matrix composites. Mater Today Commun 2022:104855.
[16] Yang ZY, Wang LD, Li J, Shi ZD. Lateral size effect of reduced graphene oxide on properties of copper matrix composites. Mater Sci Eng, A 2021;820:141579.
[17] Kim S, Kwon HC, Lee D, Lee HS. Enhanced thermal diffusivity of copper-based composites using copper-RGO sheets. Met Mater Int 2017;23(6):1144–9.
[18] Nazeer F, Ma Z, Xie YT, Gao LH, Malik A, Khan MA, et al. A novel fabrication method of copper-reduced graphene oxide composites with highly aligned reduced graphene oxide and highly anisotropic thermal conductivity. RSC Adv 2019;9(31):17967–74.

[19] Manrique PH, Lei XZ, Xu RY, Zhou MY, Kinloch IA, Young RJ. Copper/graphene composites: a review. J Mater Sci 2019;54(19):12236–89.
[20] Zhang X, Wu K, Liu X, Ge X, Yang W. Microstructure and mechanical properties of spark plasma sintered titanium-added copper/reduced graphene oxide composites. Mater Sci Eng Technol 2019;50(10):1262–72.
[21] Dong LL, Huo WT, Ahangarkani M, Zhang B, Zhao YQ, Zhang YS. Microstructural evaluation and mechanical properties of in-situ WC/W-Cu composites fabricated by rGO/W-Cu spark plasma sintering reaction. Mater Des 2018;160:1196–207.
[22] Chu K, Wang F, Li YB, Wang XH, Huang DJ, Zhang H. Interface structure and strengthening behavior of graphene/CuCr composites. Carbon 2018;133:127–39.
[23] Yang T, Chen WG, Yan FL, Lv HB, Fu YQ. Effect of reduced graphene oxides decorated by Ag and Ce on mechanical properties and electrical conductivity of copper matrix composites. Vacuum 2021;183:109861.
[24] Dong LL, Li L, Li X, Zhang W. Enhancing mechanisms of arc-erosion resistance for copper tungsten electrical contact using reduced graphene oxides in situ modified by copper nanoparticles. Int J Refract Met H 2022;108:105934.
[25] Biyik S, Arslan F, Aydin M. Arc-erosion behavior of boric oxide-reinforced silver-based electrical contact materials produced by mechanical alloying. J Electron Mater 2015;44(1):457–66.
[26] Biyik S, Aydin M. Fabrication and arc-erosion behavior of Ag_8SnO_2 electrical contact materials under inductive loads. Acta Phys Pol, A 2017;131(3):339–42.
[27] Biyik S, Aydin M. Investigation of the effect of different current loads on the arc-erosion performance of electrical contacts. Acta Phys Pol, A 2016;129(4):656–60.
[28] Wang YD, Gao PF, Li HW, Li YX, Zhan M. Microstructural evolution and mechanical behavior in the hot deformation of GH3128 alloy. J Mater Res Technol 2022;21:627–39.
[29] Wang QB, Wang Q, Chen RR, Wang XW, Su YQ, Fu HZ. Synchronous enhancement of hot deformation capacity and properties of Nb-24Ti-16Si-2Al alloy by composite alloying of Fe and V. Mater Sci Eng, A 2022:144223.
[30] Guan C, Chen G, Kai XZ, Cao R, Miao C, Xu ZZ, et al. Evolution of microstructure and mechanical properties of graphene nanoplates and ZrB_2 nanoparticles reinforced AA6111 composites during hot rolling deformation. J Alloys Compd 2022;920:165910.
[31] Wang KK, Li XP, Li QL, Shu JJ, Tang GY. Hot deformation behavior and microstructural evolution of particulate-reinforced AA6061/B_4C composite during compression at elevated temperature. Mater Sci Eng, A 2017;696:248–56.
[32] Deng KK, Li JC, Xu FJ, Nie KB, Liang W. Hot deformation behavior and processing maps of fine-grained SiCp/AZ91 composite. Mater Des 2015;67:72–81.
[33] Ban YJ, Zhang Y, Jia YL, Tian BH, Volinsky A, Zhang XH, et al. Effects of Cr addition on the constitutive equation and precipitated phases of copper alloy during hot deformation. Mater Des 2020;191:108613.
[34] Zhang XH, Zhang Y, Tian BH, Jia YL, Liu Y, Song KX, et al. Thermal deformation behavior of the Al_2O_3-Cu/(W,Cr) electrical contacts. Vacuum 2019;164:361–6.
[35] Zhu HJ, Tian BH, Zhang Y, Zhou M, Li YZ, Zheng XH, et al. Microstructure and electrical contact behavior of the nano-yttria-modified Cu-Al_2O_3/30Mo/3SiC composite. Nanotechnol Rev 2023;12(1):20220532.
[36] Biyik S. Influence of type of process control agent on the synthesis of Ag_8ZnO composite powder. Acta Phys Pol, A 2019;135(4):778–81.
[37] Biyik S. Effect of polyethylene glycol on the mechanical alloying behavior of Cu-W electrical contact. Material. Acta Phys Pol A 2018;134(1):208–12.
[38] Biyik S, Aydin M. Optimization of mechanical alloying parameters of Cu25W electrical contact. Material. Acta Phys Pol A 2017;132(3):909–12.
[39] Biyik S, Aydin M. The effect of milling speed on particle size and morphology of Cu25W composite powder. Acta Phys Pol, A 2015;127(4):1255–60.
[40] Mu Z, Geng HR, Li MM, Nie JL, Leng JF. Effects of Y_2O_3 on the property of copper based contact materials. Composer Part B-Eng 2013;52:51–5.
[41] Lee AY, Yang K, Anh ND, Park C, Lee SM, Lee TG, et al. Raman study of D* band in graphene oxide and its correlation with reduction. Appl Surf Sci 2021;536:147990.
[42] Shahid M, Katugampalage TR, Khalid M, Ahmed W, Kaewsaneha C, Sreearunothai P, et al. Microwave assisted synthesis of Mn_3O_4 nanograins intercalated into reduced graphene oxide layers as cathode material for alternative clean power generation energy device. Sci Rep-UK 2022;12(1):19043.
[43] Zhang JY, Liu G, Sun J. Strain rate effects on the mechanical response in multi-and single-crystalline Cu micropillars: grain boundary effects. Int J Plast 2013;50:1–17.
[44] Geng YF, Zhang Y, Song KX, Jia YL, Li X, Stock H, et al. Effect of Ce addition on microstructure evolution and precipitation in Cu-Co-Si-Ti alloy during hot deformation. J Alloys Compd 2020;842:155666.
[45] Liang SL, Zhou M, Zhang Y, Liu S, Li X, Tian BH, et al. Thermal deformation behavior of GO/CeO_2 in-situ reinforced Cu30Cr10W electrical contact material. J Alloys Compd 2022;899:163266.
[46] Kim Y, Lee J, Yeom MS, Shin JW, Kim H, Cui Y, et al. Strengthening effect of single-atomic-layer graphene in metal-graphene nanolayered composites. Nat Commun 2013;4(1):1–7.
[47] Zhu JQ, Liu X, Yang QS. Dislocation-blocking mechanism for the strengthening and toughening of laminated graphene/Al composites. Comput Mater Sci 2019;160:72–81.
[48] Sellars CM, McTegart WJ. On the mechanism of hot deformation. Acta Metall 1966;14(9):1136–8.
[49] Li LH, Liu S, Zhou M, Zhang Y, Liang SL, Huang JL, et al. Microstructure evolution of graphene reinforced Cu/CeO_2/Cr electrical contact materials under thermal deformation behavior. J Mater Res Technol 2022;18:1412–23.
[50] Wu YS, Qin XZ, Wang CS, Zhou LZ. Influence of phosphorus on hot deformation microstructure of a Ni-Fe-Cr based alloy. Mater Sci Eng, A 2019;768:138454.
[51] Huang K, Logé RE. A review of dynamic recrystallization phenomena in metallic materials. Mater Des 2016;111:548–74.
[52] Haase C, Barrales-mora LA. Influence of deformation and annealing twinning on the microstructure and texture evolution of face-centered cubic high-entropy alloys. Acta Mater 2018;150:88–103.
[53] Lei Q, Li Z, Hu WP, Meng CL, Derby B, Zhang W. Microstructure evolution and hardness of an ultra-high strength Cu-Ni-Si alloy during thermo-mechanical processing. J Mater Eng Perform 2016;25(7):2615–25.